

Synchronizing the Dynamics of a Single Nitrogen Vacancy Spin Qubit on a Parametrically Coupled Radio-Frequency Field through Microwave Dressing

S. Rohr,¹ E. Dupont-Ferrier,¹ B. Pigeau,¹ P. Verlot,¹ V. Jacques,² and O. Arcizet^{1,*}

¹*Institut Néel, CNRS et Université Joseph Fourier, 38042 Grenoble, France*

²*Laboratoire Aimé Cotton, CNRS, Université Paris-Sud and ENS Cachan, 91405 Orsay, France*

(Received 8 July 2013; revised manuscript received 13 October 2013; published 7 January 2014)

A hybrid spin-oscillator system in parametric interaction is experimentally emulated using a single nitrogen vacancy (NV) spin qubit immersed in a radio frequency (rf) field and probed with a quasiresonant microwave (MW) field. We report on the MW-mediated locking of the NV spin dynamics onto the rf field, appearing when the MW-driven Rabi precession frequency approaches the rf frequency and for sufficiently large rf amplitudes. These signatures are analogous to a phononic Mollow triplet in the MW rotating frame for the parametric interaction and promise to have impact in spin-dependent force detection strategies.

DOI: 10.1103/PhysRevLett.112.010502

PACS numbers: 03.67.-a, 42.50.Wk, 76.30.Mi

In recent years, research on mechanical hybrid systems has powered vast experimental and theoretical efforts with the counterintuitive perspectives of revealing the quantum behavior of matter at the macroscopic scale [1,2], such as the creation of nonclassical states of motion. These semi-quantum devices generally consist of a mechanical oscillator interfaced with a quantum system, such as circuit qubits [3,4], cold atoms [5], quantum dots [6–9], or single molecules [10], with which quantum state swapping is envisioned as in pioneering trapped ion experiments [11]. Because of their unique spin coherence properties [12–14], which potentially allow to enter the strong coupling regime [15,16], nitrogen vacancy (NV) defects have received important attention. In particular, the influence of mechanical motion on the spin dynamics has recently been investigated [17–19], while demonstrating the reverse interaction remains a challenging task.

Many of the advanced protocols envisioned for observing spin-dependent forces [16,20–22]—the key ingredient for nonclassical state generation—would benefit from the ability to manipulate the spin state at the mechanical oscillation frequency, permitting an enhancement of the spin-dependent force readout capacity. This represents an experimental challenge since the mechanical resonances are designed to be spectrally sharp in order to gain access to large force sensitivities enabled by high mechanical quality factors whereas the experimental control that can be obtained on the stability of a single spin precession frequency is significantly lower.

In this Letter, we emulate a hybrid spin-mechanical system by immersing a single NV spin in an external radio-frequency (rf) field that modulates the qubit energy [23,24] in analogy to a mechanical oscillator in parametric interaction with the two-level system. We report on the observation and analysis of synchronization of the single spin dynamics on the emulated mechanical oscillator motion when driven at sufficiently large amplitudes, while adjusting the microwave (MW) power to make the spin precession approach the oscillation frequency.

In this regime, the rf/mechanical modulation is dynamically imprinted on the qubit dynamics, allowing an enhanced coherent spin backaction onto the mechanical oscillator once implemented in hybrid mechanical systems. Most of the qubit-based sensing protocols, originally developed in the field of NMR on spin ensembles [25], rely on dynamical manipulation of the spin state at the frequency of the signal under investigation by combining perpendicular signal and control fields [26–29]. These techniques have been implemented in qubit environment spectroscopy or ultrasensitive sensing experiments [30–32] aimed at detecting weak signals for which the spin synchronization is not visible. The MW dressing enables the original parametric phonon coupling to be turned into a resonant interaction—the one of cavity QED [33]—where a phononic excitation generates transitions between dressed states. Since the traditional roles of σ_x and σ_z operators are interchanged in the picture of dressed states, the synchronization can be understood as a Mollow triplet signature of the parametric interaction.

Formalization.—A qubit parametrically coupled to a rf field or, similarly, a hybrid spin-mechanical system is described by the Hamiltonian [2,15] $H = H_0 + H_{\text{int}}$ with $H_0 = \hbar\omega_0\sigma_z + \hbar\Omega_m a^\dagger a + \hbar\omega b^\dagger b$ where $\hbar\omega_0$ is the qubit energy splitting, $\Omega_m/2\pi$ is the oscillator/rf frequency, and $\omega/2\pi$ is the frequency of the MW field used for spin manipulation. The a, a^\dagger and b, b^\dagger operators are annihilation and creation operators for the rf and MW fields, respectively. The interaction Hamiltonian is $H_{\text{int}} = \hbar\kappa^v(a + a^\dagger)\sigma_z + \hbar\Omega_R\sigma_x(b + b^\dagger)$. The first term describes the parametric interaction with the rf-oscillator field, κ^v being the vacuum coupling strength. For a classically driven phonon field, it can be rewritten as $\hbar\sigma_z\delta\omega_0 \cos(\Omega_m t)$, $\delta\omega_0$ describing the amplitude of the parametric energy modulation [see Fig. 1(a)]. The second term represents the MW field interaction with the spin. For a classical MW field, it can be similarly replaced by $\hbar\Omega_R\sigma_x \cos(\omega t)$ where Ω_R represents the strength of the MW field, with a detuning defined by

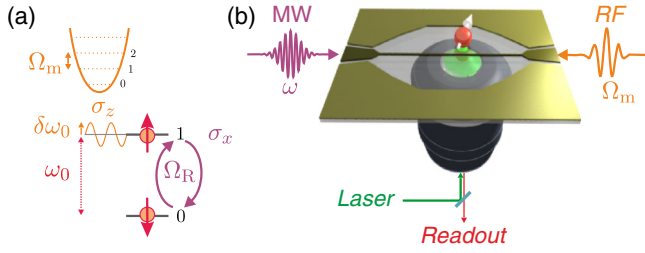


FIG. 1 (color online). An emulated spin-mechanical hybrid system. (a) A single NV spin qubit is coupled to a rf field (frequency $\Omega_m/2\pi$), which parametrically modulates its energy splitting ($\hbar\omega_0$) with an amplitude $\hbar\delta\omega_0$ while quasiresonant MW irradiation (pulsation ω) is used to manipulate the spin state, drive Rabi precessions of the two-level system (frequency $\Omega_R/2\pi$), and realize resonant spectroscopy of the system. (b) Experimental setup: a single NV defect hosted in a diamond nanocrystal deposited on a glass plate is optically read out through a confocal microscope apparatus, and the spin-state-dependent fluorescence [34] is read out on an avalanche photodiode. MW and rf fields required for spin manipulation [34] and spin energy modulation, respectively, are delivered via a coplanar waveguide (see the Supplemental Material [35]).

$\delta \equiv \omega - \omega_0$. Although the quantization of the phonon and photon fields is not formally necessary to describe our experiment where the only quantum object is the NV spin qubit, it permits for an elegant description of our findings in analogy with the appearance of Mollow triplets in dressed states spectroscopy.

Spin-rf interaction.—The parametric interaction between the rf field and the NV spin is first characterized by continuous electron spin resonance (ESR) measurements (see Fig. 2), where the fluorescence of the NV defect is recorded as a function of the applied MW frequency. In the absence of rf field [Figs. 2(a,i) and 2(c,i)] a characteristic fluorescence reduction is observed when the MW frequency

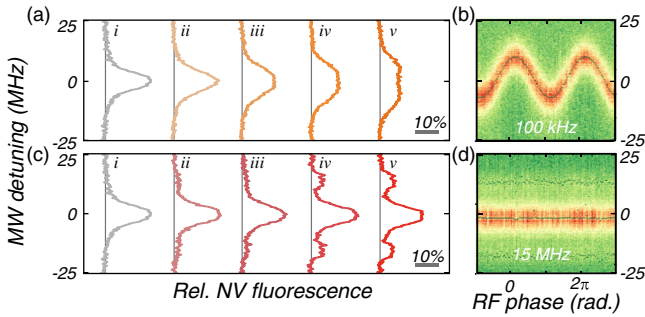


FIG. 2 (color online). Characterization of the spin-rf interaction in the adiabatic and resolved sideband regimes [$\Omega_m/2\pi = 20$ kHz in (a) and (b), 15 MHz in (c) and (d)]. Left: ESR spectra obtained in the absence of rf field (i) and for increasing oscillation amplitudes [$\delta\omega_0 = 2.5, 4.7, 6.2$, and 9.1 MHz from (ii) to (v), respectively]. Right: time-resolved ESR spectra obtained by gating the photon counts (20% duty cycle) at different rf oscillatory phases for $\delta\omega_0 = 9.1$ MHz. In the adiabatic case (b), the modulation observed has an amplitude of $\delta\omega_0$, while no temporal evolution is visible in the RSB case (d) since the spin dynamics is too slow to follow the imposed RF field.

is resonant with the spin transition. The rf field amplitude is subsequently progressively increased [(i) to (v)]. When the mechanical frequency is small enough compared to the internal spin dynamics [Fig. 2(a): $\Omega_m/2\pi = 20$ kHz], we observe a motional broadening of the spin resonance, as observed in earlier hybrid qubit-mechanical experiments [17,19,24,36]. The rf phase-gated ESR measurements synchronized on the rf modulation phase enable the observation of the spin resonance temporal evolution and measuring the energy modulation induced by the rf amplitude $\delta\omega_0$ [Fig. 2(b)]. In contrast, when the rf frequency is greater than the spin decay rate, sidebands appear on the ESR spectra. As a hallmark of frequency modulation, they are characterized by a separation corresponding to the rf oscillation frequency (15 MHz here) and a depth that initially increases with the oscillation amplitude [Figs. 2(c) and 2(d)]. The strength of the sidebands [4,23,24,37–39], defined as their relative area in order to account for MW and optical broadening [40], has been experimentally verified to follow a Bessel evolution and is in agreement with our numerical simulations of Bloch equations (see Supplemental Material [35]). The substructure especially visible in the sidebands reflects the hyperfine coupling between the NV electronic and ^{14}N nuclear spins. For the remainder of this Letter, all considerations will be restricted to the resolved sideband regime, where the mechanical oscillation frequency is greater than the spin decay rates, which have been measured at the level of $T_1 \approx 173 \mu\text{s}$ and $\Gamma_{\text{spin}} = 3 \times 10^5 \text{ s}^{-1}$ ($T_2^{\text{Rabi}} \approx 3 \mu\text{s}$) at $\Omega_R/2\pi = 5$ MHz (see Supplemental Material [35]).

Rabi maps.—In order to quantify the spin-MW interaction, we have carried out a systematic study of MW-induced Rabi oscillations of the NV qubit. The measured Rabi oscillations are shown in Fig. 3 in the absence (a) and presence (b) of rf parametric drive, and the corresponding numerical simulations can be seen in Figs. 3(c) and 3(d). The measurements performed on the non-rf-driven NV qubit are used to calibrate the Rabi frequency that presents an initial quadratic dependence in the MW detuning. When the rf drive is turned on, the structure of the Rabi map is significantly modified. Rabi oscillations can now be driven when pumping the spin on the motional sidebands by adjusting the MW detuning to $\delta = \pm\Omega_m$. The Rabi oscillation frequency Ω_R^n ($n = 0, \pm 1$) has subsequently been measured for varying MW powers (e), rf amplitudes (f), and rf frequencies (g) and compared to the equation $\Omega_R^n = \Omega_R |J_n(\delta\omega_0/\Omega_m)|$, where $J_n(x)$ is the n th-order Bessel function of the first kind. Note that these measurements have been carried out at sufficiently low MW powers so that the Rabi precession frequency remains small compared to the rf frequency. This capacity of driving coherent spin oscillations on the motional sidebands is of importance in hybrid spin-oscillator systems since the MW photon absorption simultaneously proceeds through phonon emission or absorption ($\delta = \pm\Omega_m$), which enables advanced qubit-based cooling protocols [4,16] in analogy with the laser cooling of ions [41] or optomechanical cooling [42] experiments.

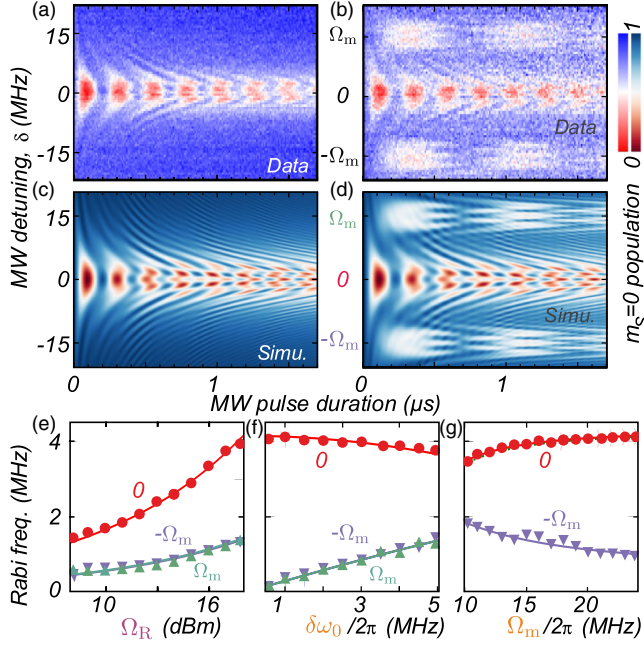


FIG. 3 (color online). Experimental [(a) and (b)] and numerically simulated [(c) and (d)] Rabi oscillations of NV spin in the presence [(b) and (d)] and absence [(a) and (c)] of rf modulation. The spin state is optically prepared in its $m_S = 0$ ground state and subsequently irradiated with a MW field whose detuning is varied across the resolved sideband spectrum of Fig. 1(c). The substructures observed at large MW pulse duration are inherent to the NV defect's hyperfine structure. Bottom: evolution of the Rabi frequency measured by tuning the MW frequency on the carrier ($\delta = 0$) or on the first sidebands ($\delta = \pm\Omega_m$) as a function of the driving amplitude Ω_R (e), oscillation amplitude $\delta\omega_0$ (f), and oscillation frequency ($\Omega_m/2\pi$) (g). When nonvaried, parameters are $\delta\omega_0/2\pi = 4.5$ MHz, $\Omega_m/2\pi = 15$ MHz, and 18 dBm MW power. Solid lines are fits based on Bessel functions and calibration measurements; see text.

In the following, the experiments are carried out at resonance ($\delta = 0$) and at the excited state level anticrossing [43,44] where electron-nuclear spins flip-flops mediate a ^{14}N nuclear spin polarization, liberating our measurements from beating frequencies due to the hyperfine coupling.

Spin synchronization.—The spin synchronization mechanism appears when the MW amplitude is chosen so that the Rabi precession approaches the rf/mechanical oscillation frequency: $\Omega_R \approx \Omega_m$. In that case and for sufficiently large rf amplitudes ($\delta\omega_0 \gtrsim \Gamma_{\text{spin}}$), the Rabi dynamics of the NV spin qubit is dramatically modified, as shown in Fig. 4(a) and in the corresponding Fourier analysis [Fig. 4(b)] where a triplet structure is observed. The synchronization of the spin precession frequency onto the rf drive frequency can be better visualized when the MW power is scanned so that the Rabi frequency is swept across the synchronization region [Fig. 4(c)]. When the Rabi frequency is sufficiently detuned from the mechanical oscillation frequency, only one single peak is visible in the FFT, corresponding to the regime explored above (Fig. 3). When increasing the MW power

to approach the synchronization region, a triplet structure appears with a dominant central component oscillating exactly at the rf frequency and a minimum half splitting of $\delta\omega_0/2$. The impossibility of generating Rabi oscillations at frequencies lying in the gaps to both sides of the central peak illustrates the spin synchronization onto the rf/mechanical field. The MW pulse sequence is intentionally not synchronized to the rf phase in these experiments. We further investigated this mechanism by varying the rf oscillation amplitude $\delta\omega_0$. As can be seen in Fig. 4(e), the triplet separation—that is, the synchronization capture region—increases linearly with the rf drive. Note that the spin locking mechanism [25], which has recently been implemented on NV and trapped ions magnetometers [30,32], is usually investigated at low rf drive amplitudes, for which spin synchronization as shown here can not be observed. Our experimental findings are in quantitative agreement with numerical simulations based on Bloch equations [Fig. 4(d)] (see the Supplemental Material [35]), except for peak linewidth. This is a consequence of the well-established non-Markovian nature of the spin bath in diamond [31], which is also responsible for the observed extended Rabi decay times [Fig. 4(a)] [45].

The synchronization mechanism can be qualitatively understood through a parametric driving of the spin precession, a virtual oscillator whose frequency depends quadratically on the MW detuning: $\Omega_R^{\text{eff}} \approx \Omega_R + \delta^2/2\Omega_R$ (see Fig. 3). The rf field modulates the detuning at Ω_m and, thus, the effective Rabi frequency at $2\Omega_m$, which falls close to twice the precession frequency in the synchronization region where $\Omega_R \approx \Omega_m$. This regime of parametric driving of the Rabi precession generates an amplified spin precession at half the parametric modulation frequency Ω_m , which is then locked onto the rf field [see Fig. 4(f)] with a capture frequency range increasing with the drive amplitude $\delta\omega_0$ [see Fig. 4(e)] as in classical parametric driving of oscillators. This interpretation is of course limited, since the complex qubit dynamics on the Bloch sphere can not be fully reproduced in this simplified description.

Doubly dressed qubit interpretation.—The spin locking mechanism can be better interpreted by considering the qubit as being doubly dressed with MW and rf fields. We first proceed with a MW dressing of the spin qubit [33], resulting in a new energy ladder of dressed states $|\pm_N\rangle$, of energy splitting $\Omega_R^v\sqrt{N}$ increasing with the parametrized photon number N . In case of large coherent MW drive, the study can be restricted to the dressed states associated with the coherent state mean photon number whose splitting amounts to Ω_R (see the Supplemental Material [35]). This direct manifestation of the MW dressing represents a new effective two-level system [see Fig. 4(g)], at the origin of the Autler-Townes doublet [46], between which the σ_z operator (the one precisely involved in the hybrid coupling Hamiltonian) has nonzero matrix elements. The synchronization mechanism then appears as a consequence

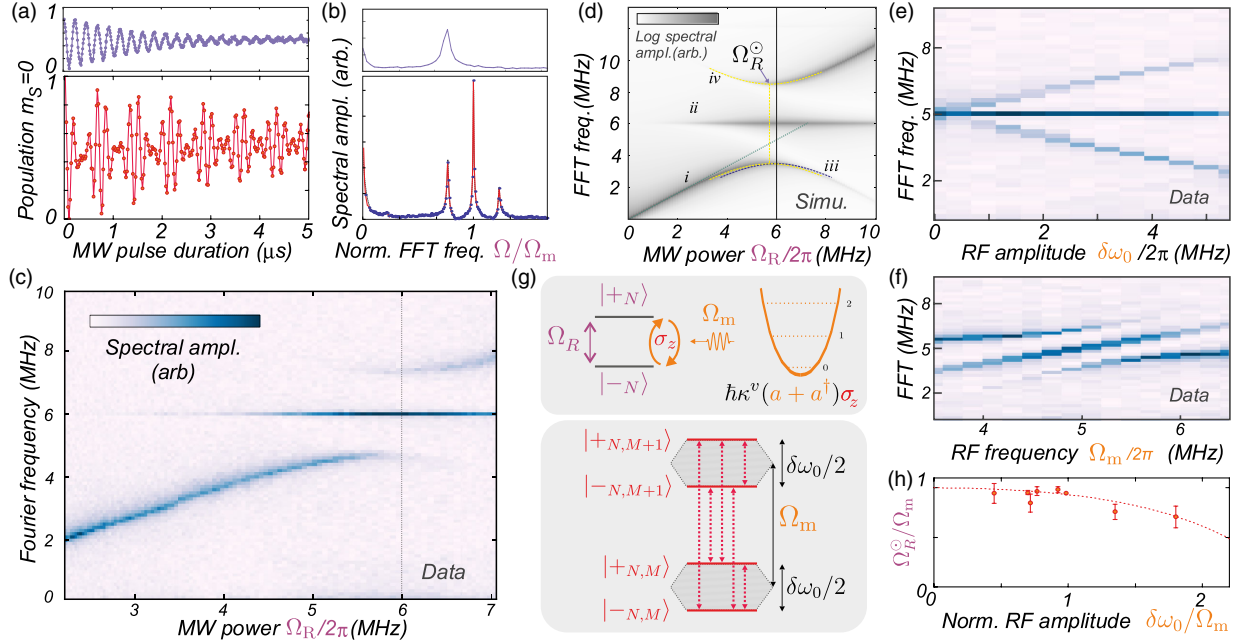


FIG. 4 (color online). Spin synchronization. Rabi oscillations (a) and their corresponding FFT spectra (b) measured for resonant MW pumping ($\delta = 0$) in the absence (above) or presence (below) of rf modulation at a frequency close to the Rabi precession: $\Omega_R \approx \Omega_m$ (5/6 MHz here). The triplet structure is the signature of spin locking, which is more easily evidenced in [(c) and (d)] experimental and simulated FFT spectra of the Rabi oscillations for varying MW power to scan the Rabi precession frequency across the rf/mechanical resonance. In the spin locking region, a gap appears in the energy spectrum of spin dynamics. (e) FFT spectra measured at the synchronization point ($\Omega_R = \Omega_m$) for increasing rf amplitudes $\delta\omega_0$. (f) Variation of the mechanical frequency across the synchronization point for fixed MW power ($\Omega_R/2\pi = 5$ MHz) and rf amplitude $\delta\omega_0/2\pi = 2.7$ MHz. (g) Interpretation of the synchronization mechanism in term of rf dressing of the MW dressed qubit. Transitions between doubly dressed states are detectable as frequency components of Rabi oscillations Ω_m , $\Omega_m \pm \delta\omega_0/2$. (h) “rf light shifts”: dependence on the oscillation amplitude of MW powers Ω_R° , which minimizes the triplet splitting. The dashed lines represent sixth-order expansions of the Bloch-Siegert light shifts (see text), whereas data points are derived from eight measurements similar to panel (c).

of rf/mechanical phonon parametric interaction with the MW-dressed qubit, which permits a second rf dressing step. This generates a new set of multiplicities that are now parametrized by the phonon number M inside of which the new eigenstates $|\pm_{N,M}\rangle$ are linear combinations of product states $|\pm_N\rangle|M\rangle$ [see Fig. 4(g)]. For strong coherent rf fields, the energy splitting can be expressed as $\Delta = \sqrt{(\Omega_R - \Omega_m)^2 + \delta\omega_0^2/4}$. The experimentally measured FFT spectra of Rabi oscillations can be obtained by calculating the spectrum of the σ_z operator within the doubly dressed states. In analogy with the Mollow triplet in quantum electrodynamics, the Rabi oscillations spectrum will contain signals at the mechanical frequency Ω_m but also sidebands at $\Omega_m \pm \Delta$, as indeed observed in the experimental spectra of Fig. 4(b). Note that the Mollow triplet structure is only visible for large rf/mechanical fields, for which $\delta\omega_0/2 > \Gamma_{\text{spin}}$. Since no synchronization is required for observing the triplet structure, these signatures are expected to persist with mechanical motion of reduced temporal coherence such as Brownian motion or zero-point fluctuations for sufficiently high coupling strength.

rf light shifts.—To fully explain the experimental observations, the rotating wave approximation that is implicitly

done in the dressing procedure is not entirely justified since the rf driving amplitudes $\delta\omega_0$ can be of a magnitude equal to the mechanical frequency Ω_m (corresponding to the ultrastrong coupling regime). Indeed, one can clearly see from the experimental data [Fig. 4(c)] but also from numerical simulations [Fig. 4(d)] that the MW power Ω_R° for which the triplet structure presents the smallest energy splitting is slightly lower than Ω_m . This is a direct signature of the “light shifts” or Bloch Siegert effect [28,47] of the rf field on the MW-dressed spin qubit. We have carried out a numerical and experimental analysis of the rf light shifts through the dependence of Ω_R° in the rf oscillation strength [see Fig. 4(h) and the Supplemental Material [35]], which are in good agreement with the analytical expansion in $\delta\omega_0/\Omega_m$ of QED light shifts [47].

In conclusion, the synchronization criteria $\Omega_m \approx \Omega_R$ and $\Omega_m, \delta\omega_0/2 > \Gamma_{\text{spin}}$ can be achieved in state of the art implementations. For example, a $50 \times 0.05 \mu\text{m}$ SiC nanowire oscillating at 1 MHz [15,17,22] with a 3 nm rms amplitude at 300 K and a 700 fm zero point motion allows achieving coupling strengths ($\delta\omega_0, \kappa^v$) of (80 MHz, 20 kHz), respectively, once immersed in strong magnetic field gradients of 10^6 T/m [20]. Finally, our findings demonstrate how MW

dressing rotates the perspective in the Bloch sphere dynamics and transforms a parametric interaction into a resonant coupling between the mechanical oscillator and the dressed states so that one can expect the wealth of cavity QED experimental signatures [33,48] to be transposed to qubit-mechanical hybrid systems in parametric interaction.

We thank C. Fabre, O. Buisson, A. Auffeves, G. Nogues, D. Feinberg, S. Seidelin, M. Dartailh, C. Hoarau, and D. Lepoitevin, for theoretical, experimental, and technical assistance. This project is supported by a Marie Curie reintegration grant, an ANR RPDoc program, and the ERC Starting Grant HQ-NOM. S.R. acknowledges funding from the Nanoscience Foundation.

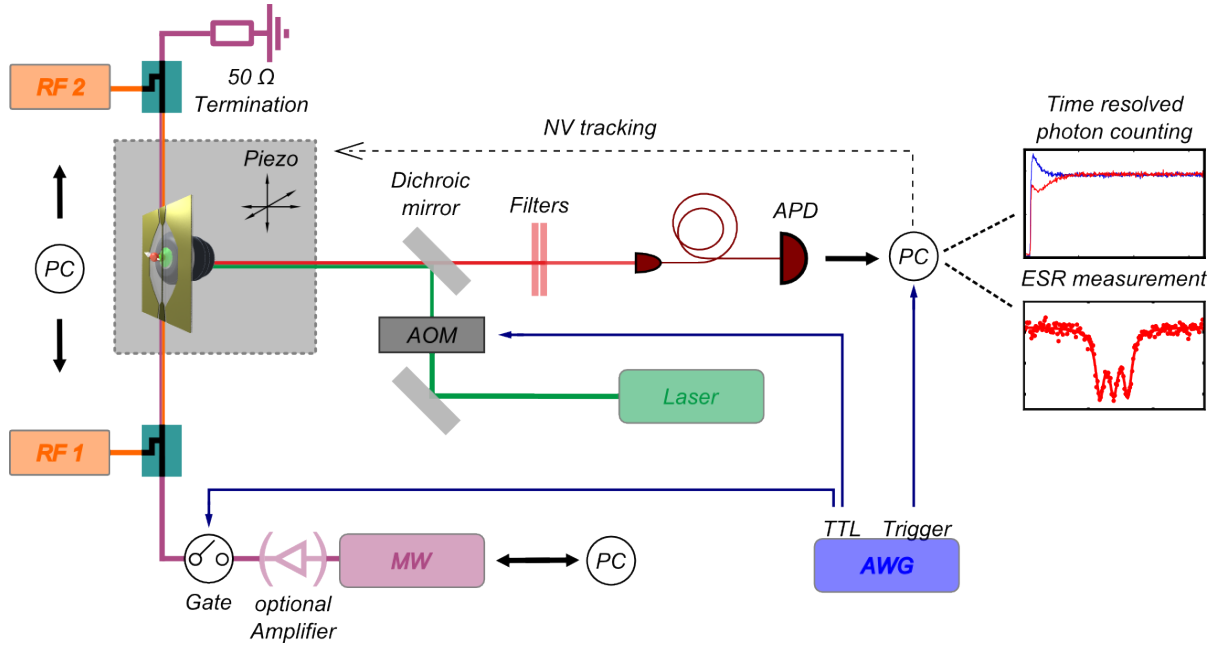
*olivier.arcizet@neel.cnrs.fr

- [1] K. C. Schwab and M. L. Roukes, *Phys. Today* **58**, 7, 36 (2005).
- [2] P. Treutlein, C. Genes, K. Hammerer, M. Poggio, and P. Rabl, in *Cavity Optomechanics*, edited by M. Aspelmeyer, T. Kippenberg, and F. Marquardt (Springer, New York, to be published), [arXiv:1210.4151](https://arxiv.org/abs/1210.4151).
- [3] M. D. LaHaye, J. Suh, P. M. Echternach, K. C. Schwab, and M. L. Roukes, *Nature (London)* **459**, 960 (2009).
- [4] J.-M. Pirkkalainen, S. U. Cho, J. Li, G. S. Paraoanu, P. J. Hakonen, and M. A. Sillanpää, *Nature (London)* **494**, 211 (2013).
- [5] P. Treutlein, D. Hunger, S. Camerer, T. W. Hansch, and J. Reichel, *Phys. Rev. Lett.* **99**, 140403 (2007).
- [6] B. Lassagne, Y. Tarakanov, J. Kinaret, D. Garcia-Sanchez, and A. Bachtold, *Science* **325**, 1107 (2009).
- [7] G. Steele, A. K. Huttel, B. Witkamp, M. Poot, H. B. Meerwaldt, L. P. Kouwenhoven, and H. S. J. van der Zant, *Science* **325**, 1103 (2009).
- [8] G. Sallen, A. Tribu, T. Aichele, R. André, L. Besombes, C. Bougerolc, S. Tatarenko, K. Kheng, and J. Ph. Poizat, *Phys. Rev. B* **80**, 085310 (2009).
- [9] S. D. Bennett, L. Cockins, Y. Miyahara, P. Grütter, and A. A. Clerk, *Phys. Rev. Lett.* **104**, 017203 (2010).
- [10] M. Ganzhorn, S. Klyatskaya, M. Ruben, and W. Wernsdorfer, *Nat. Nanotechnol.* **8**, 165 (2013).
- [11] R. Blatt and D. J. Wineland, *Nature (London)* **453**, 1008 (2008).
- [12] R. Hanson, O. Gywat, and D. D. Awschalom, *Phys. Rev. B* **74**, 161203 (2006).
- [13] L. Childress, M. V. G. Dutt, J. M. Taylor, A. S. Zibrov, F. Jelezko, J. Wrachtrup, P. R. Hemmer, and M. D. Lukin, *Science* **314**, 281 (2006).
- [14] G. Balasubramanian *et al.*, *Nat. Mater.* **8**, 383 (2009).
- [15] P. Rabl, P. Cappellaro, M. Dutt, L. Jiang, J. R. Maze, and M. Lukin, *Phys. Rev. B* **79**, 041302 (2009).
- [16] P. Rabl, *Phys. Rev. B* **82**, 165320 (2010).
- [17] O. Arcizet, V. Jacques, A. Siria, P. Poncharal, P. Vincent, and S. Seidelin, *Nat. Phys.* **7**, 879 (2011).
- [18] S. D. Bennett, S. Kolkowitz, Q. P. Unterreithmeier, P. Rabl, A. C. B. Jayich, J. G. E. Harris, and M. D. Lukin, *New J. Phys.* **14**, 125004 (2012).
- [19] S. Hong, M. S. Grinolds, P. Maletinsky, R. L. Walsworth, M. D. Lukin, and A. Yacoby, *Nano Lett.* **12**, 3920 (2012).
- [20] D. Rugar, R. Budakian, H. J. Mamin, and B. W. Chui, *Nature (London)* **430**, 329 (2004).
- [21] C. L. Degen, M. Poggio, H. J. Mamin, C. T. Rettner, and D. Rugar, *Proc. Natl. Acad. Sci. U.S.A.* **106**, 1313 (2009).
- [22] J. M. Nichol, E. R. Hemesath, L. J. Lauhon, and R. Budakian, *Phys. Rev. B* **85**, 054414 (2012).
- [23] L. Childress and J. McIntyre, *Phys. Rev. A* **82**, 033839 (2010).
- [24] J. Li *et al.*, *Nat. Commun.* **4**, 1420 (2013).
- [25] C. P. Slichter, *Principles of Magnetic Resonance* (Springer, Heidelberg, 1996).
- [26] S. A. Holmstrom, C. Wei, A. S. M. Windsor, N. B. Manson, J. P. D. Martin, and M. Glasbeek, *Phys. Rev. Lett.* **78**, 302 (1997).
- [27] S. A. Holmstrom, A. S. M. Windsor, C. Wei, J. P. D. Martin, and N. B. Manson, *J. Lumin.* **76**, 38 (1998).
- [28] A. R. Saiko and G. Fedoruk, *JETP Lett.* **87**, 128 (2008).
- [29] A. P. Saiko and R. Fedaruk, *JETP Lett.* **91**, 681 (2010).
- [30] S. Kotler, N. Akerman, Y. Glickman, A. Keselman, and R. Ozeri, *Nature (London)* **473**, 61 (2011).
- [31] G. deLange, D. Ristè, V. V. Dobrovitski, and R. Hanson, *Phys. Rev. Lett.* **106**, 080802 (2011).
- [32] M. Loretz, T. Roskopf, and C. L. Degen, *Phys. Rev. Lett.* **110**, 017602 (2013).
- [33] S. Haroche and J. M. Raimond, *Exploring the Quantum* (Oxford University Press, New York, 2006).
- [34] F. Jelezko, T. Gaebel, I. Popa, A. Gruber, and J. Wrachtrup, *Phys. Rev. Lett.* **92**, 076401 (2004).
- [35] See the Supplemental Material at <http://link.aps.org/supplemental/10.1103/PhysRevLett.112.010502> for a detailed description of the setup as well as a theoretical derivation of the double dressing.
- [36] S. Kolkowitz, A. C. B. Jayich, Q. P. Unterreithmeier, S. D. Bennett, P. Rabl, J. G. E. Harris, and M. D. Lukin, *Science* **335**, 1603 (2012).
- [37] V. Puller, B. Lounis, and F. Pistolesi, *Phys. Rev. Lett.* **110**, 125501 (2013).
- [38] W. D. Oliver, Y. Yu, J. C. Lee, K. K. Berggren, L. S. Levitov, T. P. Orlando, *Science* **310**, 1653 (2005).
- [39] E. Dupont-Ferrier, B. Roche, B. Voisin, X. Jehl, R. Wacquez, M. Vinet, M. Sanquer, and S. De Franceschi, *Phys. Rev. Lett.* **110**, 136802 (2013).
- [40] A. Dreau, M. Lesik, L. Rondin, P. Spinicelli, O. Arcizet, J.-F. Roch, and V. Jacques, *Phys. Rev. B* **84**, 195204 (2011).
- [41] D. Leibfried *et al.*, *Nature (London)* **422**, 412 (2003).
- [42] A. Schliesser, O. Arcizet, R. Rivière, G. Anetsberger, and T. J. Kippenberg, *Nat. Phys.* **5**, 509 (2009).
- [43] V. Jacques, P. Neumann, J. Beck, M. Markham, D. Twitchen, J. Meijer, F. Kaiser, G. Balasubramanian, F. Jelezko, and J. Wrachtrup, *Phys. Rev. Lett.* **102**, 057403 (2009).
- [44] B. Smeltzer, J. McIntyre, and L. Childress, *Phys. Rev. A* **80**, 050302 (2009).
- [45] J.-M. Cai, B. Naydenov, R. Pfeiffer, L. P. McGuinness, K. D. Jahnke, F. Jelezko, M. B. Plenio, and A. Retzker, *New J. Phys.* **14**, 113023 (2012).
- [46] S. H. Autler and C. H. Townes, *Phys. Rev.* **100**, 703 (1955).
- [47] C. Cohen-Tannoudji, J. Dupont-Roc, and C. Fabre, *J. Phys. B* **6**, L214 (1973).
- [48] J. J. Sanchez-Mondragon, N. B. Narozhny, and J. H. Eberly, *Phys. Rev. Lett.* **51**, 550 (1983).

Supplemental Material : Synchronizing the Dynamics of a Single Nitrogen Vacancy Spin Qubit on a Parametrically Coupled Radio-Frequency Field through Microwave Dressing

1 Measurement setup

NV centers are inclusions in nanodiamonds spincoated on a quartz plate. We measure the fluorescence of a single NV center with the setup shown in S1. Manipulation of the NV center is performed by MW and RF fields applied through a home-made coplanar waveguide deposited on the quartz plate.



S 1: Setup. A confocal microscope is employed to read and prepare the NV electronic spin state. MW and RF currents are combined in a homemade duplexer and delivered to the NV via a coplanar waveguide lithographed on a quartz plate supporting diamond nanocrystals.

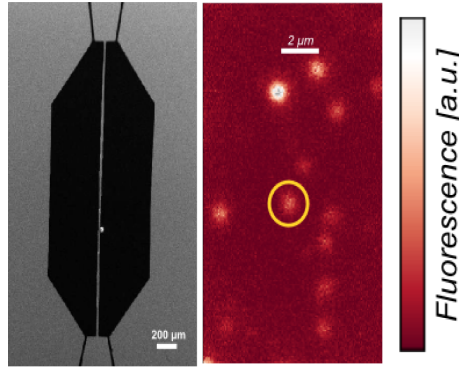
The NV fluorescence is excited non-resonantly with a 532nm laser. The photons emitted by the NV center are collected via a high numerical aperture microscope objective ($NA = 0.85$, compensated for 200 μm glass thickness) and sent through two optical filters to an avalanche photo diode (APD) (see S1). Fluorescence rates detected by the APD are in the 20 kHz range for the NV center used in this article. Measurements of Rabi oscillations were done in the saturated regime in order to be insensitive to intensity fluctuations of the laser. A 200 MHz AOM is used to form laser pulses for initialization and time-resolved readout of the NV center's spin state.

The microscope objective is mounted on a piezo-stage in order to track a single NV center. We developed a

tracking program with a feedback loop which continuously maximizes the NV fluorescence. An adaptative step size routine allows for tracking a single NV over long duration while minimizing the fluorescence fluctuations due to the tracking.

For all the experiments described in the paper we restrict ourselves to the states $|m_S = -1\rangle$ and $|m_S = 0\rangle$. A permanent magnet is used to Zeeman split the NV states $|m_S = -1\rangle$ and $|m_S = +1\rangle$ and to reach the ESLAC. To address NV centers with MW and RF fields we patterned a home-made $50\,\Omega$ impedance coplanar waveguide on the quartz plate sample. On the central part of the waveguide an optical window is opened to allow optical access to the NV centers for fluorescence measurements. In this part the central conductor dimensions are reduced (cross section $27\,\mu\text{m} \times 0.15\,\mu\text{m}$) in order to increase locally the magnetic field (see S2).

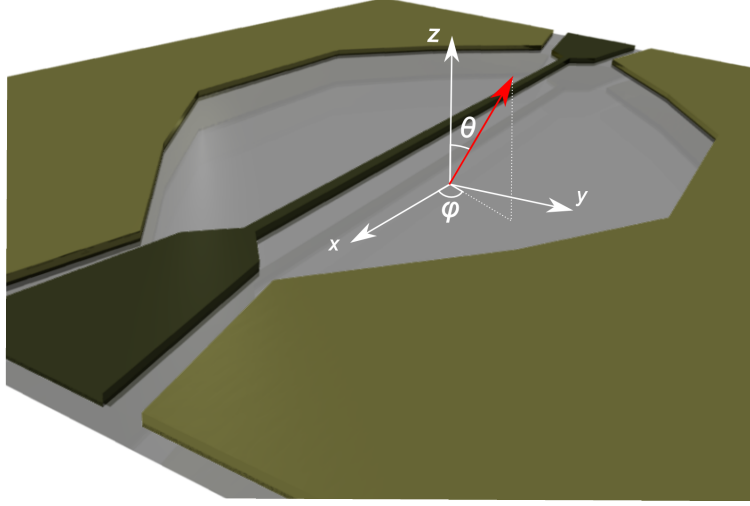
Using the Biot-Savart law we estimate the local magnetic field seen by a NV center located $5\,\mu\text{m}$ away from the waveguide (see S. 2) and with a spin orientation perpendicular to the quartz plane to be $0.235\,\text{mT/V}$, with V the applied bias voltage. The corresponding shift of the ESR resonance frequency is given by $\beta^{\text{max}} = \frac{g\mu_B}{h} \frac{B}{V} \sim 6.58\,\text{MHz/V}$.



S 2: Waveguide. Left: Electron microscope image of the waveguide used in this experiment. Right: Fluorescence scanning image of a collection of NV centers close to the waveguide. The NV center circled in yellow is the one used in this study.

2 Determination of the orientation of the NV center

Since the NV centers used in the experiment are hosted in nanodiamonds spin coated onto the sample, their alignment relative to the quartz plate is not under control. We determine the orientation of our NV center by approaching a permanent magnet with a homogeneous field gradient from two directions and detecting the corresponding Zeeman shift of the ESR peak. For the NV center presented in the main text, the polar angle (the angle between the optical axis (z) and the NV quantization axis) is estimated at $\theta \approx 68^\circ$, while the azimuthal angle (the angle between the waveguide central conductor axis (x) and the projection of the NV quantization axis onto the quartz plate, see S. 3) is estimated at $\phi \approx 71^\circ$. The imprecision inherent to the determination of the absolute magnetic field applied generates a 10% error for this estimation. The magnetic field B generated by the waveguide in the vicinity of the NV center is perpendicular to the quartz plate (Biot-Savart calculations show that the slight elevation of the waveguide and the vertical uncertainty in the nanocrystal position play negligible roles here), we have $B_{\parallel} = B \cos \theta$ and $B_{\perp} = B \sin \theta$. Hence, our NV center will experience magnetic field contributions along both directions, where components oscillating along B_{\parallel} will modulate the energy of the NV center and B_{\perp} will induce spin rotations.



S 3: NV orientation. The schematics shows the orientation of the NV quantization axis with respect to the waveguide axis ($\parallel \hat{x}$) and the optical axis ($\parallel \hat{z}$) with angles θ and ϕ .

For the experiments presented in the main text MW and RF fields are simultaneously applied through the same waveguide. As described in [1] the effects of the magnetic fields (both Rf and MW) can be categorized as follows:

- $B_{\parallel}^{\text{RF}}$: energy modulation of the two level system (TLS) at RF frequencies.
- B_{\perp}^{RF} : RF frequencies are off-resonant and hence do not induce spin transitions.
- $B_{\parallel}^{\text{MW}}$: Energy modulation at MW frequencies are too rapid compared to all other time-scales involved to be seen by the TLS.
- B_{\perp}^{MW} : Will induce spin transitions at resonance.

Note that in order for multi-photon spin transitions to occur between $|m_S = 0\rangle$ and $|m_S = -1\rangle$ (which could have been responsible for Rabi oscillations on the sidebands (Fig. 3 in the article)), an odd number of photons needs to be absorbed / emitted by the TLS in order to preserve the spin selection rules for the interaction Hamiltonian. Such effects for photon numbers larger than 1 are highly unlikely and thus neglected in our further considerations [1]. As a consequence, we can restrict our study to the Hamiltonian described in the article, where the RF and MW fields play an asymmetric role: the RF modulates the spin energy (σ_z), while the MW induces spin flips (σ_x).

3 Modeling of the NV spin dynamics in presence of RF and MW fields

For all measurements presented in the main text a static magnetic field is applied in order to Zeeman shift the levels $|m_S = -1\rangle$ and $|m_S = +1\rangle$ and restrict ourselves to the $S^{(\frac{1}{2})}$ subspace : ($|m_S = 0\rangle, |m_S = -1\rangle$), discarding the $|m_S = +1\rangle$ state. We thus model the NV center as a single two level system with spin states $|0\rangle$ and $|1\rangle$ coupled to a MW field via the σ_x -operator and to a RF field via the σ_z -operator, as justified in the previous section. The restriction to the subspace leads to a rescaling of the magnetic fields if we want to use the convenient spin 1/2 formalism in our Hamiltonian which can be rewritten: $H_{\text{int}}/g\mu_B = B_{\parallel}\sigma_z^{1/2} + B_{\perp}/\sqrt{2}\sigma_x^{1/2}$. Thus, the fields become $B_{\parallel}^{(\frac{1}{2})} = B_{\parallel}^{(1)}$ and $B_{\perp}^{(\frac{1}{2})} = \frac{1}{\sqrt{2}}B_{\perp}^{(1)}$. This is equivalent to rescaling the parametrized MW drive strength Ω_R , such that $\Omega_R = \frac{g\mu_B}{\sqrt{2}\hbar}B_{\perp}^{\text{MW}}$.

Furthermore, we make the approximation of a Markovian environment for the spin and assume that all information

of the spin's coherence passed to the environment is completely lost. This approximation although not entirely justified for NV spins in nano-diamonds allows to understand most of the experimental traces observed. However this approximation fails when trying to explain the increase of Rabi oscillation decay time as observed in Fig 4a. This effect which can be interpreted as a continuous dynamical decoupling and a protection of the spin coherence due to the continuous spin locking is beyond the scope of this article and will be investigated elsewhere.

3.1 Bloch equations

The NV spin dynamic is described by the following system of Bloch equations [2]:

$$\begin{pmatrix} \dot{u} \\ \dot{v} \\ \dot{w} \end{pmatrix} = \begin{pmatrix} -\Gamma_2^* - \Gamma_c & -(\omega - \omega_0(t)) & 0 \\ \omega - \omega_0(t) & -\Gamma_2^* - \Gamma_c & \Omega_R/2 \\ 0 & -2\Omega_R & -2\Gamma_1 - \Gamma_p \end{pmatrix} \begin{pmatrix} u \\ v \\ w \end{pmatrix} - \begin{pmatrix} 0 \\ 0 \\ \Gamma_p \end{pmatrix} \quad (1)$$

Here, u is the real part of the dipole matrix element, v the imaginary part and w is the population difference defined as $w = \sigma_{11} - \sigma_{00}$. The involved parameters are:

- Ω_R - the strength of the microwave field,
- ω - the frequency of the microwave field,
- $\omega_0(t) = \omega_0 + \delta\omega_0 \cos(\Omega_m t + \psi)$ - the resonance frequency of the TLS, which is modulated at a frequency Ω_m by an amplitude $\delta\omega_0$, at an oscillatory phase ψ (see 6).
- Γ_1 - the population decay rate from state $|m_s = -1\rangle$ to state $|m_s = 0\rangle$
- Γ_p - the relaxation due to the optical illumination, which repolarizes the spin in its ground state [2]. This process implies a transition via the metastable state. Therefore Γ_p is limited by the lifetime of the metastable state: $\Gamma_p = \Gamma_p^\infty \frac{s}{s+1}$, where $\Gamma_p^\infty \approx \frac{1}{200 \text{ ns}} = 5 \text{ MHz}$, and $s = P_{\text{opt}}/P_{\text{sat}}$ the saturation parameter of the radiative transition given by the ratio of the optical pumping power P_{opt} and the saturation power P_{sat} .
- Γ_2^* - the intrinsic spin decoherence rate.
- Γ_c - the decoherence consequent to the destruction of phase information due to optical transitions, $\Gamma_c = \Gamma_c^\infty \frac{s}{s+1}$, where $\Gamma_c \approx \frac{1}{12 \text{ ns}} = 80 \text{ MHz}$.

3.2 Bloch equations for Rabi oscillations

For Rabi oscillations only the MW and RF fields act on the spin and the laser is turned off during the spin evolution, hence $s = 0$ and the optically induced decay rates reduce to $\Gamma_p = \Gamma_c = 0$. This simplifies equation (1) to:

$$\begin{pmatrix} \dot{u} \\ \dot{v} \\ \dot{w} \end{pmatrix} = \begin{pmatrix} -\Gamma_2^* & -(\omega - \omega_0(t)) & 0 \\ \omega - \omega_0(t) & -\Gamma_2^* & \Omega_R/2 \\ 0 & -2\Omega_R & -2\Gamma_1 \end{pmatrix} \begin{pmatrix} u \\ v \\ w \end{pmatrix} \quad (2)$$

3.3 Connection between temporal decay rates and FFT linewidths

We place ourselves here in the case of resonant driving $\delta = 0$. In absence of RF field, the decay rate of Rabi oscillations ($w(t) \propto e^{-\Gamma_2^{\text{Rabi}} t} \cos(\Omega_R t)$) is given by

$$\Gamma_2^{\text{Rabi}} = \frac{\Gamma_2^*}{2} + \Gamma_1,$$

The corresponding peak in the FFT power spectrum (see Fig. 4 for an FFT amplitude spectrum) has a half width at half maximum of $\Gamma_2^{\text{Rabi}}/2\pi$. When turning on the RF field, three peaks are now visible in the FFT amplitude

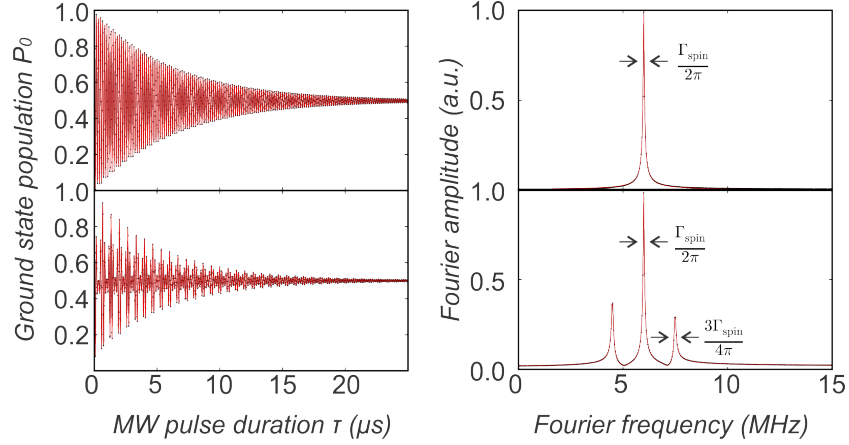
plot, splitted by $\delta\omega_0/2$. The central peak HWHM is unchanged, while the side peaks of the Mollow triplet present a 1.5 times larger damping rate (see Fig. 4). The simulated FFT amplitude spectra are fitted with the expression:

$$|A_0 + B_0 L(f, f_m, \Gamma_{\text{spin}}/2\pi) + B_+ L(f, f_m + \delta\omega_0/2, 3\Gamma_{\text{spin}}/4\pi) + B_- L(f, f_m - \delta\omega_0/2, 3\Gamma_{\text{spin}}/4\pi)|$$

where

$$L(f, f_1, \delta f) \equiv \frac{1}{f - f_1 - i\delta f}$$

is a Lorentzian whose power spectrum HWHM is δf .

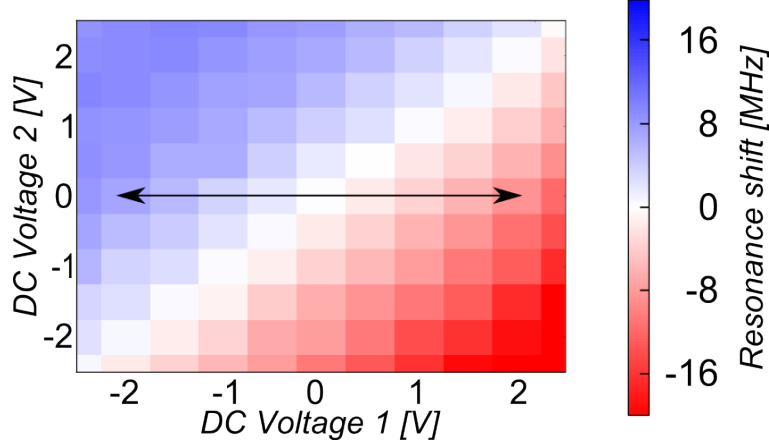


S 4: Simulated traces of Rabi oscillations and their corresponding FFT amplitude spectra, in absence and presence of a 6 MHz RF field. Black points are the results of our simulations of Bloch equations, red curve are fits (see text). The damping rate of the central peak of the triplet is the same as the one obtained in absence of RF. The side peaks of the triplet feature 1.5 times larger damping rates. In the real experiment this is not the case, due to the non-Markovian nature of the spin environment.

4 Calibration

4.1 RF-field calibration

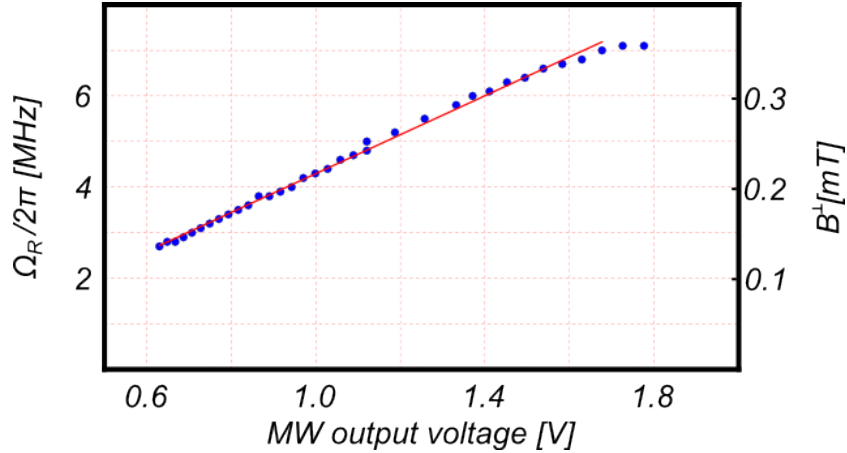
To evaluate the RF magnetic field seen by the NV center we measure how the ESR spectra are affected by the RF signals. Figure S5 shows the shifts of the ESR resonance obtained for different DC voltages applied to the waveguide input ports. The dual RF injection scheme was developed for compensating electric fields that induce quadratic shifts of the ESR frequency as a function of the applied voltage. For the NV presented in this article, increasing the DC voltage of both input channels leads to a linear shift of the ESR spectra. This firstly confirms that no residual DC field is present at the position of the NV center: indeed the shifts in the ESR spectra measured are symmetrical with respect to zero. Then, we deduce a linear dependency of the resonance shift as a function of RF amplitude voltage of $\beta = 3.6 \text{ MHz/V}$. Using the simulated value of $\beta^{\text{max}} = 6.58 \text{ MHz/V}$, we conclude that the NV center is oriented with a polar angle of $\theta = 56^\circ (\pm 3^\circ)$, which is in rough agreement with the measurements of section 2, the difference originating from the local structure of the waveguide and the impedance imperfections of the RF ports scheme.



S 5: RF calibration map. The scan along two directions allows to verify the linear shift of the spin resonance with the applied voltage. The arrow indicates the modulation axis of the experiments presented here.

4.2 MW-field calibration

To calibrate the amplitude of the microwave field seen by the NV center, we measure Rabi oscillations for varying MW input powers, see section 5.2. We verify that the measured Rabi frequency Ω_R varies linearly with the amplitude of the microwave generator output, as expected for a two level system. Using the previous expressions for Rabi frequencies (taking into account the spin 1 to spin 1/2 reduction), the corresponding magnetic field seen by the NV center falls in the range between 0.1 mT and 0.35 mT. The transmission losses in the MW port are estimated below 3 dB, rendering the use of MW power amplifiers unnecessary, which improves the long term stability of the MW scheme. This was found to be critical for accumulating Rabi traces over several days in order to obtain high quality FFT data on a single electronic spin, as presented in this paper. The NV employed in this article was chosen to present sufficient RF and MW sensitivities.

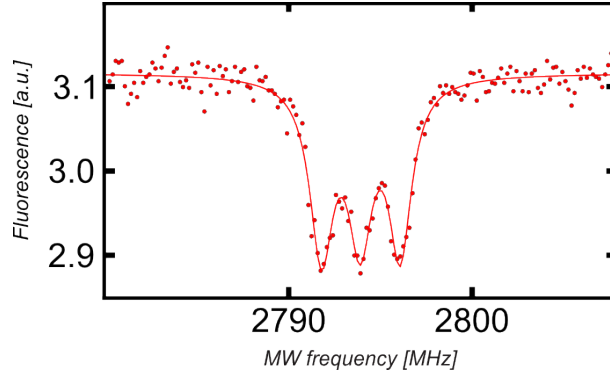


S 6: MW coupling. The MW calibration measurement (blue dots) allows to quantify Ω_R vs. injected MW power. The red line is a linear fit.

5 Measurements

5.1 ESR and hyperfine structure

Figure S7 shows the ESR spectra obtained at low microwave power (3 dBm) and in presence of a small static magnetic field of $B_{\parallel}^{\text{ext}} \approx 2.4$ mT which lifts the degeneracy between $|m_S = -1\rangle$ and $|m_S = +1\rangle$ states. The ESR peak, corresponding to the transitions between $|m_s = 0\rangle$ and $|m_s = -1\rangle$, exhibits a well resolved substructure of three peaks of width 1.4 MHz and 2.2 MHz separation. This substructure is a consequence [3] of the hyperfine interaction between the NV electronic and the ^{14}N nuclear spin of $I = 1$.

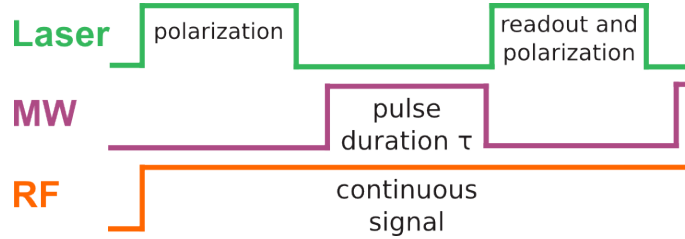


S 7: Hyperfine structure. A measurement showing the hyperfine structure in the ESR response of the NV defect under investigation.

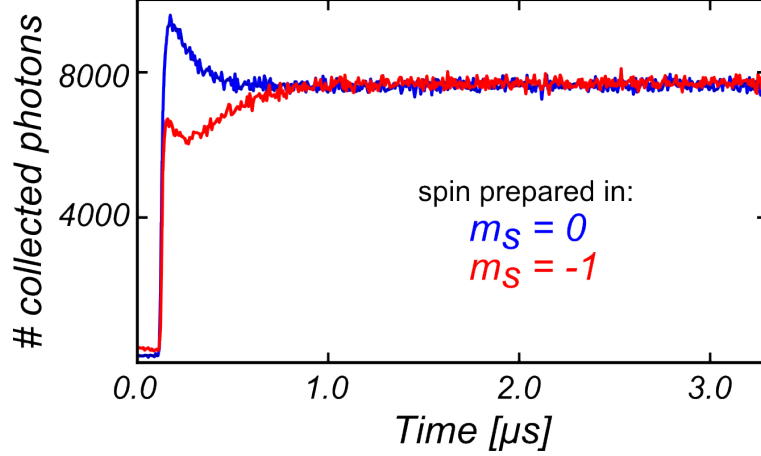
This hyperfine coupling is responsible for the subpeak structures observed in the Rabi maps in Fig. 3 and has been taken into account in the simulations (see section 6).

5.2 Rabi oscillations

We measure Rabi oscillations following the protocol depicted in figure S8: First the NV spin is initialized in its ground state $|0\rangle$ with a $5\ \mu\text{s}$ laser pulse, then the NV spin-state is manipulated with MW pulses of variable duration τ . Finally the spin state is read out by applying a laser pulse and measuring the spin-dependant fluorescence signal [4]. The emitted photons are detected by correlated photon counting measurement synchronized to the Rabi sequence, using a P7889 Multiscaler from FastComTek, see S9. Using relatively long laser pulses in our protocols allows maintaining significant amount of optical duty cycles in order to maintain a sufficiently large photon number to guarantee the reliability of the NV tracking.

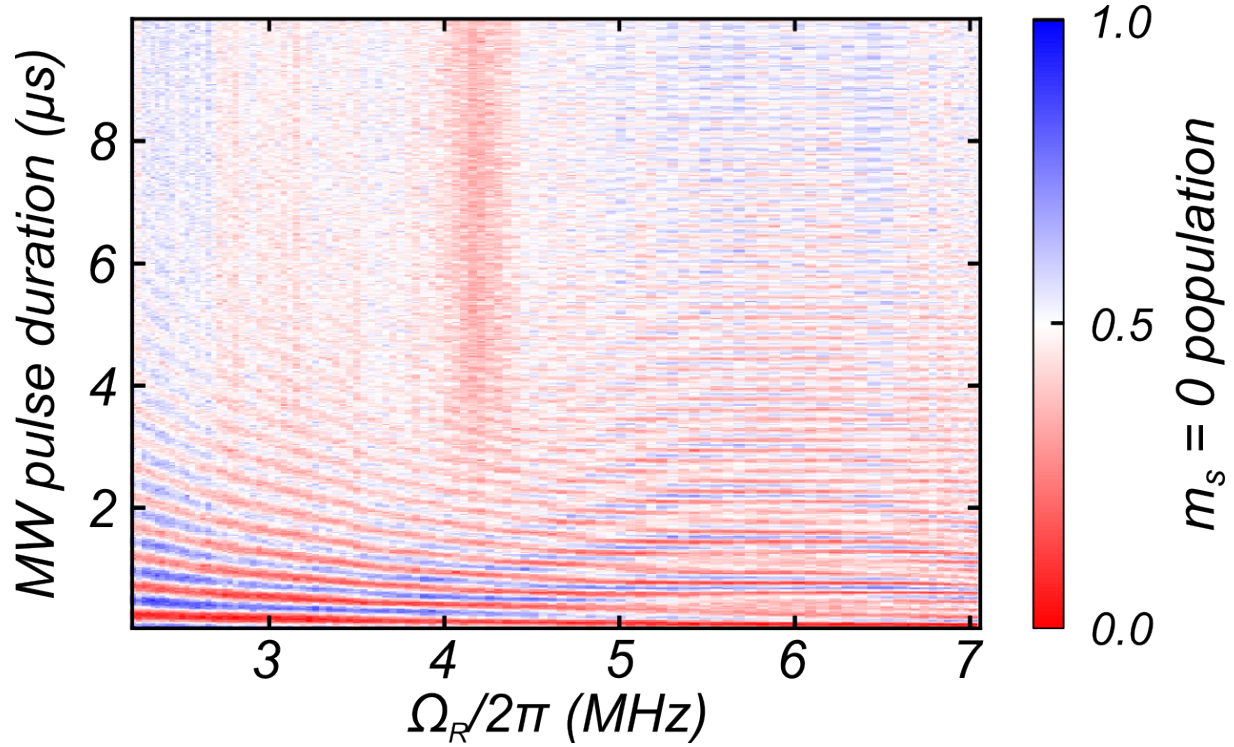


S 8: Rabi oscillation sequence. The spin is optically polarized and subsequently manipulated by the microwave field. The following laser pulse serves to readout the spin state and re-polarizes the spin prior to the next MW pulse. In our protocol, the RF field is permanently turned on.



S 9: Spin dependent fluorescence. The NV prepared in $|0\rangle$ (blue trace) emits on average more photons than the NV prepared in $|1\rangle$ (red trace).

Measurements of Rabi oscillations presented in Fig. 3 and 4 of the main text are the result of an average over 1.4×10^6 realizations and correspond to about 40 hours of continuous measurement. During this duration the position of the NV center with respect to the confocal microscope is kept constant by the home made NV-tracking program. To compensate temporal drifts of the ESR resonance due to changes in temperature or drift of the external dc magnetic field for measurements in Fig. 4, an ESR measurement is performed and the MW frequency is re-set to resonance for each new set of experimental parameters. The temporal traces used to build the FFT map of Fig. 4c are shown in S 10, clearly demonstrating the interplay of the different frequency components in terms of beating signatures as well as the enhanced coherence times T_2^{Rabi} . Notice however, that the measurement in Fig. 4b was done by continuous data acquisition over approximately 120 h, emphasizing the role of spin synchronization in compensating drifts of the MW drive strength.

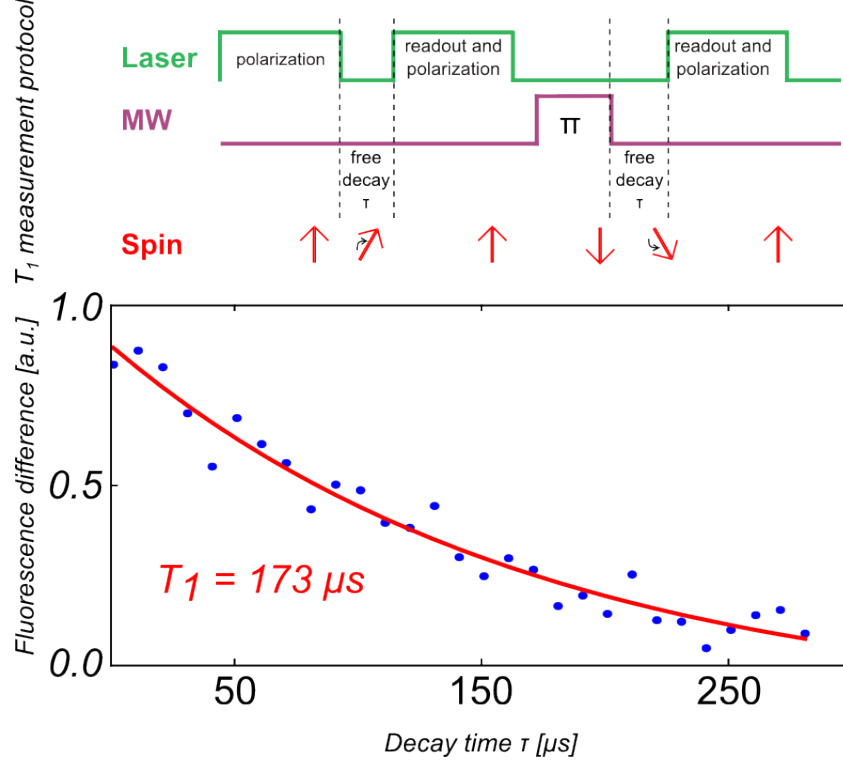


S 10: Temporal traces of Rabi oscillations for varying MW powers. The plot represents the temporal evolution of the spin population corresponding to the FFT traces of Fig. 4c, where $\Omega_m/2\pi = 6$ MHz.

To obtain sufficiently large resolution on the discrete Fourier transform spectra of Fig. 4e, 4f of the article, Rabi oscillations are measured for MW pulse duration varying between 20 ns and 5 μ s in 10 ns steps corresponding to a spectral resolution of 200 kHz. The data used for Fig. 4c correspond to [20 ns - 10 μ s] in 20 ns steps (100 kHz resolution). The high resolution data of Figure 4a and 4b correspond to the range [20 ns - 20 μ s] in 20 ns steps (50 kHz resolution).

5.3 T_1 measurements

The lifetime of the excited spin state is measured by polarizing the NV center in its excited state $|1\rangle$ or in its ground state $|0\rangle$ and measuring the population after a varying time interval τ as described in [5]. The NV is initialized in state $|0\rangle$ by optical pumping and then for every second measurement point rotated to $|1\rangle$ by a MW π -pulse (while τ stays the same), see S11. The population is then read out by optical means and fitted to an exponential decay. We find a population lifetime of $T_1 = 173 \mu$ s, as depicted in S11.



S 11: T_1 measurement. Fitting to an exponential decay yields $T_1 = 173 \mu s$. Inset: protocol and schematics of the spin evolution

5.4 T_{spin} measurements

The measured decay rate of Rabi oscillations depends on the experimental conditions, even if analytical solutions of (1) predict that in case of resonant driving ($\delta = 0$), the MW power does not contribute to the decay time of Rabi oscillations. Indeed, our measurements indicate that it slightly decreases with the MW drive strength, an effect that can not be described in our model where a Markovian bath has been employed. For example, the measurements of S6 indicates that the decay rate of Rabi oscillations follows the expression: $\Gamma_2^{\text{Rabi}} \approx 0.37 + 0.11(\Omega_R/2\pi) \text{ s}^{-1}$, Ω_R in MHz. One can see that in the spin synchronization regime which requires large Rabi frequencies, the spin linewidth, called Γ_{spin} for simplicity in the article, remains small compared to the RF frequency. For the measurements of Fig 4a,b taken in slightly different conditions due to longer time scans, the Rabi decay rate was measured at the level of $\Gamma_{\text{spin}} \approx 3 \times 10^5 \text{ s}^{-1}$. In the article we have also employed the term Γ_{spin} when describing the modulated ESR signatures and defining the resolved sideband regime. In that case, one has to take into account the additional light broadening (Γ_c) but for simplicity we have chosen to keep the same notation.

6 Simulations

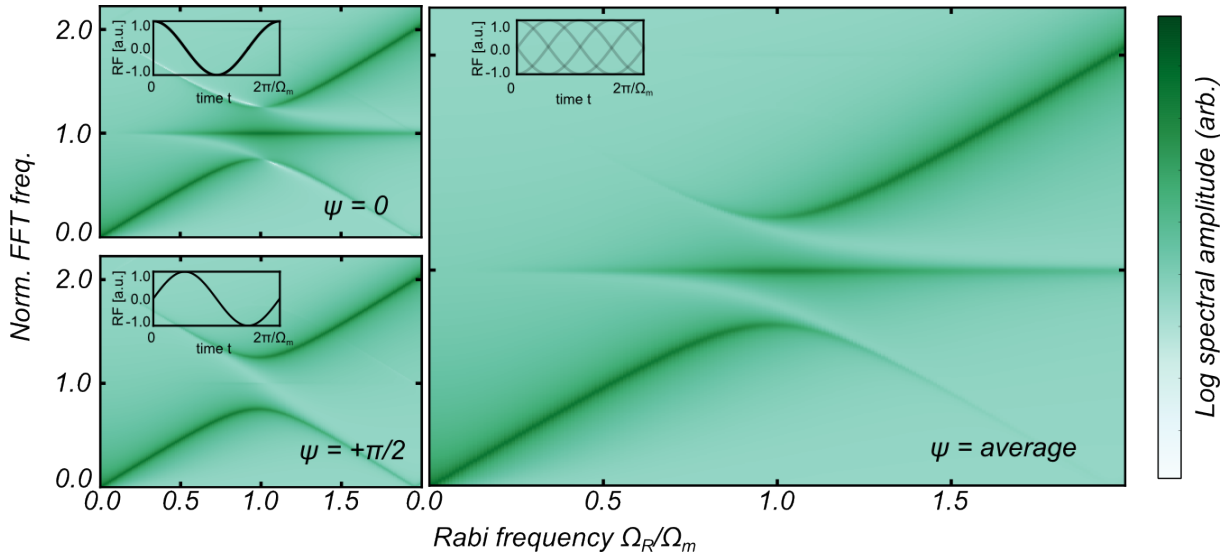
To simulate the Rabi maps presented in Fig. 3 and 4 of the main text, we solved the system of equations (2) numerically using a Runge-Kutta algorithm of 4th order developed in C. In our simulations, we use a temporal stepsize of $10^{-4} \mu s$. The initial parameters for the spin are $w(t=0) = -1$, and $u(t=0) = v(t=0) = 0$ meaning that the system is fully polarized in state $|0\rangle$ at time $t=0$. Other parameters are $\Gamma_1 = 6000 \text{ s}^{-1}$, $\Gamma_2^* = 3 \times 10^5 \text{ s}^{-1}$.

6.1 Hyperfine structure

The peaked substructure observed on the experimental maps of Fig. 3 is due to the hyperfine coupling (cf section 5.1) and was implemented in our simulations. The nuclear spin lifetime is significantly longer (~ 10 ms in [6]) than a single MW pulse duration in the sequence of the Rabi protocol, but far shorter than the whole accumulation time (hours). Thus we can consider that our measurements reflect the average over all possible nuclear spin configurations. As a consequence, the final Rabi maps of Fig. 3 were obtained by superposing three maps simulated for ω_0 , $\omega_0 - 2.1$ MHz and $\omega_0 + 2.1$ MHz.

6.2 RF phase averaging

No synchronization between the RF field and the Rabi sequence was employed in the experiments. However, in our simulations the oscillatory phase at which the laser pulse is turned off, initializing the system evolution in presence of RF and MW fields starting from the $|0\rangle$ state, do play a role as in classical phase lock loops. The derived FFT spectra thus strongly depend on the oscillatory phase, ψ , as can be seen in figure S12. When the NV is driven at $\Omega_R = \Omega_m$, the frequency component at Ω_m is only present in the FFT for $\psi = 0[\pi]$, where simultaneously, the components at $\Omega_m \pm \delta\omega_0/2$ vanishes. Here, the phase difference ψ is defined such that for $\psi = 0$ at $t = 0$ the spin is polarized in state $|0\rangle$ and the oscillator is at maximum amplitude, corresponding to $\omega_0(t = 0) = \omega_0 + \delta\omega_0$. In the simulated maps of Fig. 4 we averaged the temporal Rabi traces over ψ before calculating the FFT map. This explains why all components are visible in the spectra.



S 12: Influence of the RF oscillatory phase on the Rabi maps. The FFT maps on the left are taken at different initial oscillation states: the left upper trace are obtained when the RF field is maximum at $t = 0$ ($\psi = 0$), the lower ones when it is at zero ($\psi = \pi/2$). The right map is obtained by averaging over the oscillatory phase in order to describe the experimental situation.

7 Doubly dressed spin

In order to understand the features of Fig. 3 and Fig. 4 of the article, we present an interpretation in term of double dressing of our system with a MW and a RF field. We find that by probing the MW dressed spin with the RF field we can explain the triple peak features and the "anti-crossing" in the FFT spectra. Reversely, this picture also leads to an explanation of the Bessel-like dependence of the effective Rabi frequency. We consider the total

Hamiltonian:

$$H_{\text{tot}} = H_0 + H_{\text{MW}} + H_{\text{int}} \quad (3)$$

with

$$\begin{aligned} H_0 &= \hbar\omega_0\hat{\sigma}_z + \hbar\Omega_{\text{m}}\hat{a}^\dagger\hat{a} + \hbar\omega\hat{b}^\dagger\hat{b} \\ H_{\text{MW}} &= \hbar\Omega_R^v(\hat{b}^\dagger + \hat{b})\sigma_x \\ H_{\text{int}} &= \hbar\kappa^v(\hat{a}^\dagger + \hat{a})\sigma_z \end{aligned}$$

The generic eigenstates of H_0 are $|m_s, N, M\rangle$, where $m_s = 0, 1$ is the spin state, N the photon number and M the phonon number. Their eigenenergies are:

$$E_{|m_s, N, M\rangle}/\hbar = m_s\omega_0 + N\omega + M\Omega_{\text{m}}.$$

7.1 Dressing the spin with the MW field

We first dress the system with the microwave field and apply H_{MW} . It does not modify the phonon number, so we can use the usual dressed atom equations: we introduce the multiplicities

$$\mathcal{E}_N = \{|1, N-1\rangle, |0, N\rangle\},$$

where N is the number of total excitations. If $\delta \equiv \omega - \omega_0$, we have an interaction Hamiltonian in the subspace:

$$H_{\text{int}}^{\text{MW}} = \begin{pmatrix} 0 & \frac{\Omega_R^v\sqrt{N}}{2} \\ \frac{\Omega_R^v\sqrt{N}}{2} & \delta \end{pmatrix},$$

where the factor of $\frac{1}{2}$ arises from the rotating wave approximation. The new eigenstates are now $|\pm_N\rangle$ with energies (setting the energy of the ground state $|0, 0\rangle$ to $\hbar\omega/2$):

$$E_{|\pm_N\rangle}/\hbar = N\omega - \frac{\delta}{2} \pm \frac{1}{2}\sqrt{\delta^2 + N\Omega_R^v{}^2}$$

featuring a splitting of

$$\Delta(N) \equiv \sqrt{\delta^2 + N\Omega_R^v{}^2}.$$

If we define the angle Θ_N in $[0, \pi]$ by :

$$\tan \Theta_N = -\Omega_R^v\sqrt{N}/\delta,$$

then the eigenstates can be written as:

$$\begin{aligned} |+_N\rangle &= \cos \frac{\Theta_N}{2} |1, N-1\rangle + \sin \frac{\Theta_N}{2} |0, N\rangle \\ |-_N\rangle &= -\sin \frac{\Theta_N}{2} |1, N-1\rangle + \cos \frac{\Theta_N}{2} |0, N\rangle. \end{aligned}$$

The σ_z operator has no effect between multiplicities having a different N and is described in the basis $\{|-_N\rangle, |+_N\rangle\}$ by:

$$\sigma_z|_{\mathcal{E}_N} = \begin{pmatrix} \sin^2 \frac{\Theta_N}{2} & -\cos \frac{\Theta_N}{2} \sin \frac{\Theta_N}{2} \\ -\cos \frac{\Theta_N}{2} \sin \frac{\Theta_N}{2} & \cos^2 \frac{\Theta_N}{2} \end{pmatrix}.$$

Importantly, this point shows that the σ_z operator now has some non-trivial action on the new dressed eigenstates. Thus, the RF field described by H_{int} can induce rotations of the dressed spin.

7.2 Dressing the MW-dressed spin state with the RF field

As mentioned in the main text, in the picture of dressed states the role of longitudinal and transversal magnetic field components are interchanged, as the dressed spin is polarized along an axis in the equatorial plane of the Bloch sphere. Hence, a magnetic field along the z direction oscillating at frequency Ω_m can induce transitions between the dressed states if the field is resonant with the energy splitting, Ω_R .

We add the phonon field and the generic eigenstates are now of the form: $|\pm_N\rangle \otimes |M\rangle \equiv |\pm_N, M\rangle$. The interaction Hamiltonian couples the eigenstates that present a phonon number difference of ± 1 and we can thus restrict our considerations to the multiplicity:

$$\tilde{\mathcal{E}}_{N,M} = \{|+N, M-1\rangle, |-N, M\rangle\}.$$

The uncoupled energies are:

$$E_{|\pm_N, M\rangle}/\hbar = N\omega - \frac{\delta}{2} \pm \frac{\Delta(N)}{2} + M\Omega_m$$

and using $\sin \Theta_N = -\Omega_R^v \sqrt{N}/\sqrt{\delta^2 + N\Omega_R^{v2}}$, the interaction Hamiltonian can be written in the multiplicity $\tilde{\mathcal{E}}_{N,M}$ as:

$$\begin{pmatrix} 0 & \kappa_{N,M}/2 \\ \kappa_{N,M}/2 & \Omega_m - \Delta(N) \end{pmatrix} \quad (4)$$

with

$$\kappa_{N,M} \equiv -\frac{\kappa^v \sqrt{M}}{2} \sin \Theta_N = \frac{\kappa^v \sqrt{M}}{2} \frac{\Omega_R^v \sqrt{N}}{\sqrt{\delta^2 + N\Omega_R^{v2}}}.$$

The new eigenstates $|\pm_{N,M}\rangle$ have energies

$$E_{|\pm_{N,M}\rangle}/\hbar = N\omega - \frac{\delta}{2} + \frac{\Delta(N)}{2} + (M - \frac{1}{2})\Omega_m \pm \frac{1}{2}\Delta(N, M), \quad (5)$$

where

$$\Delta(N, M) \equiv \sqrt{(\Omega_m - \Delta(N))^2 + \kappa_{N,M}^2}$$

and

$$\begin{aligned} |+_{N,M}\rangle &= \cos \frac{\Theta_M}{2} |+N, M-1\rangle + \sin \frac{\Theta_M}{2} |-N, M\rangle \\ |-_{N,M}\rangle &= -\sin \frac{\Theta_M}{2} |+N, M-1\rangle + \cos \frac{\Theta_M}{2} |-N, M\rangle \end{aligned}$$

and

$$\tan \Theta_M = -\kappa_{N,M}/(\Omega_m - \Delta(N)).$$

For a classical description of the MW and RF field, $\sqrt{N}\Omega_R^v \rightarrow \Omega_R$, $\sqrt{M}\kappa_{N,M}^v \rightarrow \delta\omega_0$, the splitting becomes $\Delta(N, M) \rightarrow \Delta_{\text{Mollow}}$, with

$$\Delta_{\text{Mollow}} = \sqrt{\left(\Omega_m - \sqrt{\delta^2 + \Omega_R^2}\right)^2 + \left(\frac{\delta\omega_0}{2}\right)^2 \frac{\Omega_R^2}{\delta^2 + \Omega_R^2}}.$$

In case of resonant pumping $\delta = 0$, it simplifies to:

$$\Delta_{\text{Mollow}} = \sqrt{(\Omega_m - \Omega_R)^2 + \left(\frac{\delta\omega_0}{2}\right)^2}. \quad (6)$$

The frequencies that are present in the Rabi oscillations have to be found in the spectrum of allowed transitions of the σ_z operator between the eigenstates of the doubly dressed spin. The FFT spectra of the temporal Rabi traces can be interpreted as a result of a "fluorescence cascade" of the doubly dressed spin. The observed frequency components are thus transitions allowed by the selection rules of the σ_z -operator, see S 13:

$|+_{N,M+1}\rangle \leftrightarrow |-_{N,M}\rangle$ oscillating at $\Omega_m + \Delta(N, M)$

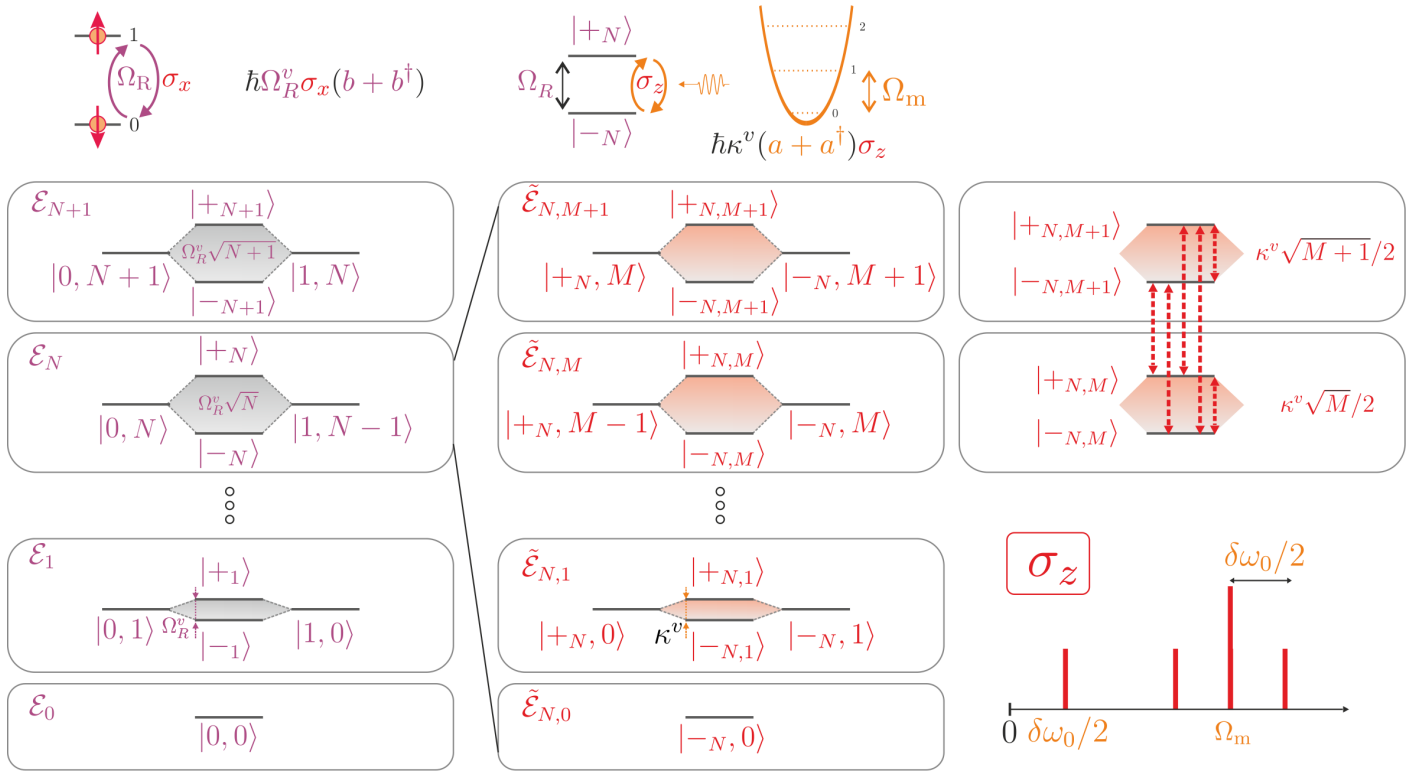
$|-_{N,M+1}\rangle \leftrightarrow |-_{N,M}\rangle$ oscillating at Ω_m

$|+_{N,M+1}\rangle \leftrightarrow |+_{N,M}\rangle$ oscillating at Ω_m

$|-_{N,M+1}\rangle \leftrightarrow |+_{N,M}\rangle$ oscillating at $\Omega_m - \Delta(N, M)$

$|+_{N,M}\rangle \leftrightarrow |-_{N,M}\rangle$ oscillating at $\Delta(N, M)$

The last term is not visible in case of perfect resonant pumping ($\delta = 0$). Due to state preparation in the ground state of the spin, our system is displaced from equilibrium at $t = 0$. Thus the analysis of its relaxation towards equilibrium following this initial displacement, which is a sort of percussional response, reveals all the allowed transitions previously calculated. Their relative weight can be computed following the previous reasoning.



S 13: Left: the spin is first dressed by the MW field. Center: the oscillator/RF field acting in the dressed base. Right: the transitions contributing to the measured Rabi oscillations close to the mechanical frequency.

7.3 Bloch - Siegert shift

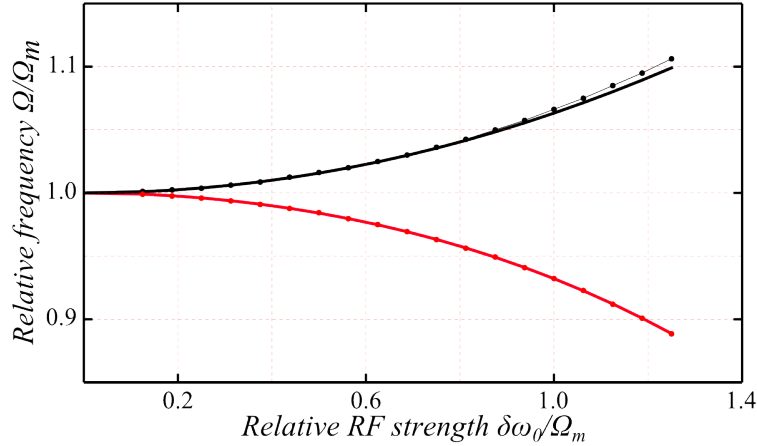
When restricting the considered transitions to the ones within multiplicities $\tilde{\mathcal{E}}_{N,M}$ we have implicitly made a rotating wave approximation (RWA) for the RF field, as reflected by the factors of $1/2$ in the off-diagonal elements of Hamiltonian (4). Here, the assumption that $\delta\omega_0 \ll \Omega_m$ is not necessarily valid and for large values of $\delta\omega_0$ we have to consider effects like the Bloch - Siegert shift for the phonon field, which is indeed visible in our simulations and experimental data, as mentioned in the main text. According to [7] the minimum splitting between the perturbed energy eigenstates occurs at $\Omega_R = \Omega_R^\odot$, with

$$\Omega_R^\odot \equiv \Omega_m - \frac{\left(\frac{\delta\omega_0}{4}\right)^2}{\Omega_m} - \frac{5\left(\frac{\delta\omega_0}{4}\right)^4}{4\Omega_m^3} + \frac{61\left(\frac{\delta\omega_0}{4}\right)^6}{32\Omega_m^5}. \quad (7)$$

We define Ω_R^* as the MW power for which the FFT component of the σ_z operator oscillating at the mechanical frequency is maximum. Its expression is given by inverting the previous equation [7]:

$$\Omega_R^* \equiv \Omega_R + \frac{\left(\frac{\delta\omega_0}{4}\right)^2}{\Omega_R} + \frac{\left(\frac{\delta\omega_0}{4}\right)^4}{4\Omega_R^3} - \frac{36\left(\frac{\delta\omega_0}{4}\right)^6}{32\Omega_R^5}. \quad (8)$$

These expressions are in quantitative agreement with simulations and in qualitative agreement with experimental data, see S 14.



S 14: Effect of the Bloch - Siegert shift. The MW power required for reaching the minimum splitting (Ω_R^\odot , red) and the maximum spectral density (Ω_R^* , black) at Ω_m depends on the RF drive amplitude. The dots are data points obtained from numerical simulations and fat solid lines are the analytical expressions given above.

References

- [1] Lilian Childress and Jean McIntyre. Multifrequency spin resonance in diamond. *Physical Review A*, 82(3), September 2010.
- [2] A. Dréau, M. Lesik, L. Rondin, P. Spinicelli, O. Arcizet, J.-F. Roch, and V. Jacques. Avoiding power broadening in optically detected magnetic resonance of single NV defects for enhanced dc magnetic field sensitivity. *Physical Review B*, 84(19):1–8, November 2011.
- [3] S. Felton, A. Edmonds, M. Newton, P. Martineau, D. Fisher, D. Twitchen, and J. Baker. Hyperfine interaction in the ground state of the negatively charged nitrogen vacancy center in diamond. *Physical Review B*, 79(7):1–8, February 2009.
- [4] F. Jelezko, T. Gaebel, I. Popa, A. Gruber, and J. Wrachtrup. Observation of Coherent Oscillations in a Single Electron Spin. *Physical Review Letters*, 92(7):1–4, February 2004.
- [5] A. Jarmola, V. Acosta, K. Jensen, S. Chemerisov, and D. Budker. Temperature- and Magnetic-Field-Dependent Longitudinal Spin Relaxation in Nitrogen-Vacancy Ensembles in Diamond. *Physical Review Letters*, 108(19):1–5, May 2012.

- [6] M V Gurudev Dutt, L Childress, L Jiang, E Togan, J Maze, F Jelezko, A S Zibrov, P R Hemmer, and M D Lukin. Quantum register based on individual electronic and nuclear spin qubits in diamond. *Science (New York, N.Y.)*, 316(5829):1312–6, June 2007.
- [7] C Cohen-Tannoudji, J Dupont-Roc, and C Fabre. Quantum calculation of the higher order terms in the Bloch-Siegert shift. *J. Phys. B: Atom. Molec. Phys.*, 6(August):214–217, 1973.